MDPI

Article

Seasonal Variability of Arctic Mid-Level Clouds and the Relationships with Sea Ice from 2003 to 2022: A Satellite Perspective

Xi Wang [1,2,3], **Jian Liu** [1,2,3,*] **and Hui Liu** [1,2,3]

1 National Satellite Meteorological Center (National Center for Space Weather), China Meteorological Administration, Beijing 100081, China; wangxi@cma.cn (X.W.); liuhui@cma.cn (H.L.)
2 Key Laboratory of Radiometric Calibration and Validation for Environmental Satellites, National Satellite Meteorological Center (National Center for Space Weather), China Meteorological Administration, Beijing 100081, China
3 Innovation Center for FengYun Meteorological Satellite (FYSIC), Beijing 100081, China
* Correspondence: liujian@cma.cn

Abstract: Mid-level clouds play a crucial role in the Arctic. Due to observational limitations, there is scarce research on the long-term evolution of Arctic mid-level clouds. From a satellite perspective, this study attempts to analyze the seasonal variations in Arctic mid-level clouds and explore the possible relationships with sea ice changes using observations from the hyperspectral Atmospheric Infrared Sounder (AIRS) over the past two decades. For mid-level clouds of three layers (648, 548, and 447 hPa) involved in AIRS, high values of effective cloud fraction (ECF) occur in summer, and low values primarily occur in early spring, while the seasonal variations are different. The ECF anomalies are notably larger at 648 hPa than those at 548 and 447 hPa. Meanwhile, the ECF values at 648 hPa show a clear reduced seasonal variability for the regions north of 80°N, which has its minimum coefficient of variation (CV) during 2019 to 2020. The seasonal CV is relatively lower in the regions dominated by Greenland and sea areas with less sea ice coverage. Analysis indicates that the decline in mid-level ECF's seasonal mean CV is closely correlated to the retreat of Arctic sea ice during September. Singular value decomposition (SVD) analysis reveals a reverse spatial pattern in the seasonal CV anomaly of mid-level clouds and leads anomaly. However, it is worth noting that this pattern varies by region. In the Greenland Sea and areas near the Canadian Arctic Archipelago, both CV and leads demonstrate negative (positive) anomalies, probably attributed to the stronger influence of atmospheric and oceanic circulations or the presence of land on the sea ice in these areas.

Keywords: mid-level clouds; Arctic; seasonal variability; sea ice; AIRS

1. Introduction

Clouds, with a coverage of approximately 66% on average globally, have a significant impact on the Earth's radiation budget through solar and thermal spectral ranges [1]. Among them, mid-level clouds account for approximately 10% to 30% [2–4], which is a substantial proportion of the total cloud cover. Mid-level clouds play a crucial role in the energy balance and vertical profile of heating in the atmosphere due to their unique height and complex phase. Understanding the formation and variations of mid-level clouds is crucial for weather forecasting, studying climate change, and assessing the accuracy of climate models.

For the polar regions, mid-level clouds have significant research values. Mid-level cloud amounts are generally less than both low- and high-level cloud amounts, except in the polar regions. As one moves from lower latitudes to higher latitudes, there is a progressive rise in the quantity of mid-level clouds [5]. Researchers utilize observations from in situ observation, satellite, radar, lidar, and atmospheric probes to monitor and

analyze the characteristics of mid-level clouds. Previous studies have indicated that mid-level clouds demonstrate distinct characteristics in polar regions, involving differences such as occurrence frequency, cloud phase, and vertical features of clouds. It has been found that based on the observations from Cloud–Aerosol Lidar and Infrared Pathfinder Satellite Observations (CALIPSO), thin mid-level clouds at night demonstrate higher frequencies than during daytime, which is more notable in the polar regions [6]. Based on airborne observations of the microstructure of low and mid-level clouds in the Beaufort Sea, evidence indicates that these clouds typically exhibit lower droplet concentrations and relatively larger effective droplet radii [7]. The one-year observations during the Surface Heat Budget of the Arctic Ocean (SHEBA) project have shown that liquid was discovered as high as 6.5 km as a combination of all-liquid and mixed-phase clouds [8]. Estimates for cloud occurrence fractions, vertical distributions, temporal persistence, diurnal cycles, boundary statistics [9], and even cloud phase [10] have further been analyzed using the cloud measurements from six Arctic atmospheric observatories over the past decade. Studies have shown that in general, the cloud occurrence fraction exhibits a peak near the surface and gradually decreases as altitude increases into the mid- and upper levels [9]. Cloud liquid water has been observed as high as 7–8 km, always associated with cloud ice at altitudes above approximately 3 km, where mid-level clouds are dominant [10]. Detailed comparisons also revealed certain differences in the occurrence and phase states of mid-level clouds among different stations and seasons, along with possible reasons [9–12]. However, due to observational conditions and limitations in measurements, there is very limited research on mid-level clouds in the Arctic region compared to the number of studies of mid-level clouds in the mid-latitude or tropic [3,13–18]. Particularly, there are few studies available on the long-term evolution of mid-level clouds in the Arctic region.

Space-borne active sensors, such as CloudSat or CALIPSO, could provide relatively accurate vertical distributions of clouds. The observations from CloudSat and/or CALIPSO have been applied to study the characteristics of mid-level clouds in the Arctic [5,6,19], but they are limited only for a case study or a timespan of less than a decade long. At the same time, the CloudSat or CALIPSO observation data of the footprint properties also affect the spatial representativeness of the research results. Since the launch of the hyperspectral Atmospheric Infrared Sounder (AIRS) aboard the Aqua satellite in 2002, there has been a significant improvement in the ability to quantitatively assess the vertical structure of the atmosphere and clouds from space [20–23]. Studies have utilized AIRS observations to analyze the long-term variability of clouds and the related parameters in the Arctic region, further exploring the possible inner connections with sea ice changes [24–26]. However, there are rare studies focusing on the long-term variations in mid-level clouds in the Arctic. In this study, the primary objective is to investigate mid-level clouds in the Arctic region utilizing nearly 20 years of AIRS data. We conducted a systematic analysis of the seasonal variations in mid-level clouds in the Arctic, and attempted to explore possible connections between mid-level cloud changes and Arctic sea ice variability. Section 2 primarily introduces the data and the relevant methods. Section 3 begins by presenting preliminary validation results for the vertical cloud fraction retrieved from AIRS in the Arctic region. Subsequently, it provides the analysis results of mid-level clouds in the Arctic, along with their potential relationships with sea ice changes. Discussions and conclusions are then provided in Sections 4 and 5.

2. Materials and Methods

2.1. Cloud Fraction Data

The data used for the following analysis are from the AIRS Version 7 (V7) Level 3 (L3) products, which are generally divided into two different types: standard and support products. The AIRS L3 standard product contains gridded retrieved parameters on the standard pressure levels roughly matching instrument vertical resolution. It has two temporal resolutions including daily and monthly. The monthly L3 product, representing the arithmetic mean of the daily L3 product, is applied here to address the long term trend

analysis and low-frequency climate variability [27]. The parameter applied in this study is the effective cloud fraction (ECF). The ECF is a combination of cloud fraction and cloud emissivity, which is retrieved following an assumption that the cloud is gray [28]. The parameter is defined as "FineCloudFrc" in AIRS L3 standard product, representing the ECF at mid-layer pressures of the 12 fine cloud layers including 1018, 887, 771, 648, 548, 447, 346, 274, 224, 173, 122, and 32 hPa. The layer boundaries are at 1100, 925, 850, 700, 600, 500, 400, 300, 250, 200, 150, 100, and 10 hPa [27,29]. The cloud product has passed the Stage 3 Validation (Val3) defined by AIRS, which means that its accuracy has been assessed and the uncertainties in the product well established via independent measurements in a systematic and statistically robust way representing global conditions [30]. The data applied here are named with suffixes of "TqJoint", which are created by a unified L2 quality control criterion for all fields to ensure that all data have the same ensembles for comparisons across levels or fields. The data, all binned into $1° \times 1°$ grid cells, are combined to be processed and analyzed both from ascending and descending orbits during the period from January 2003 to December 2022. Since the observation time difference between ascending and descending orbit data is about 12 h, the diurnal variation characteristics of the parameters can be analyzed from the ascending and descending data.

The CloudSat and CALIPSO merged (CC) cloud fraction (CF) dataset from National Center for Atmospheric Research (NCAR) is applied here for the preliminary assessment of the AIRS mid-level ECF. It is produced combining the cloud mask both from radar (dataset of 2 B-GEOPROF R04) and lidar (dataset of 2B-GEOPROF-LIDAR P2 R04) [31–33]. The data provide global (available from 82°S to 82°N) monthly gridded CF by $2° \times 2°$ cells, with a vertical resolution of 480 m. It covers the time periods from July 2006 to February 2011. No data are available polarward north of 82.5°N.

It should be noted that our interest area mainly focuses on the Arctic region north of 60°N (shown in Figure 1). However, when used for the preliminary assessment of AIRS mid-level ECF, considering the coverage area of CC observations, we selected the target area from 60° N to 82° N. The time period was concentrated between July 2006 and February 2011.
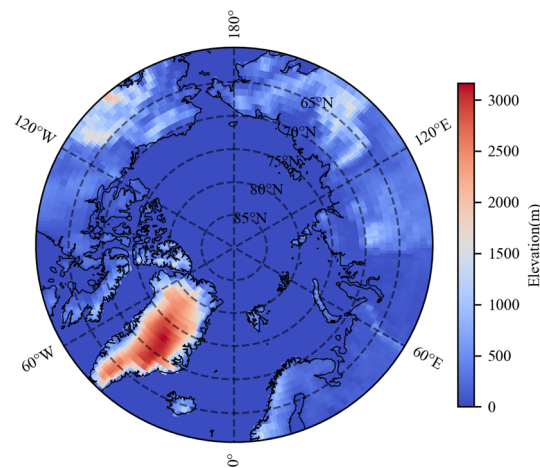

Figure 1. Study areas of the Arctic region (60–90°N) with the meridional and latitude zones for the subsequent analysis. The colored base map represents the geographic elevations.

Since AIRS vertical ECF values are given in the form of pressure layers, while CC vertical observations are expressed in terms of altitude, AIRS pressure layers need to be converted to altitude layers before comparisons. Here, the Arctic atmospheric profiles from LOWTRAN are introduced here to linearly interpolate the altitudes corresponding to the AIRS 12 fine cloud pressure layers according to the average profiles from the Arctic summer and winter standard ones. Moreover, according to the boundary altitudes (converted from the AIRS layer boundaries of 13 pressure levels) corresponding to the AIRS ECF of each layer, the mean CF of CC within the boundary altitudes is calculated to form the CC vertical

CF data with the same number of AIRS layers. Due to the fact that the definitions of ECF from AIRS and CF from CC are different, we normalize the cloud cover when comparing, that is, the proportion of CF (ECF) in each layer to the total CF (ECF) generated, which is denoted as CF (ECF) ratio Rc as (1):

$$R_c = cloud\ cover_{layer} \Big/ \sum\nolimits_{layer} cloud\ cover \tag{1}$$

Based on spatial and temporal distribution patterns, ECF/AIRS and CF/CC are compared. Figure 2 shows the comparisons of the vertical profiles between ECF of AIRS and CF of CC. The bold solid lines represent the average profile of the selected region (60°N to 82°N), while the thin lines represent the mean CF (ECF) profiles from each month during July 2006 to February 2011.
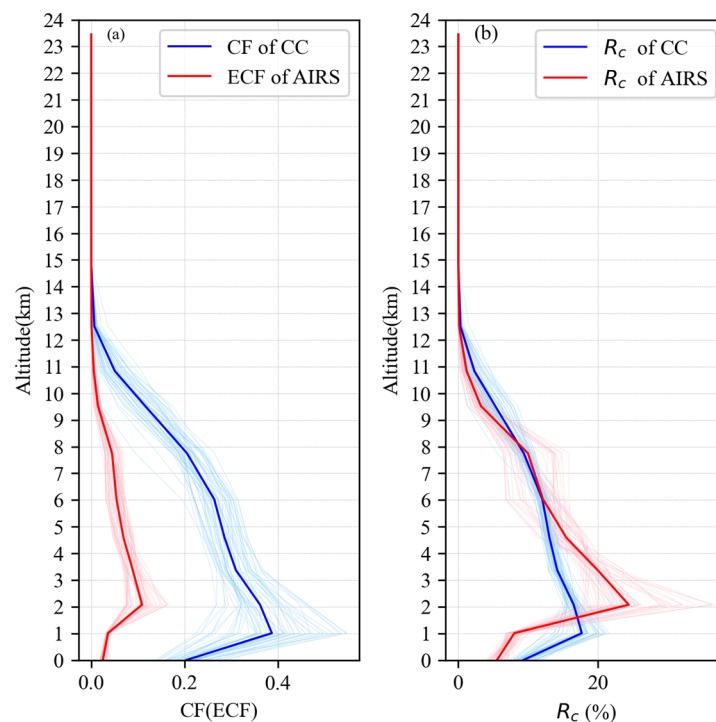

Figure 2. Comparisons of (**a**) mean vertical CF (ECF) between AIRS and CC; (**b**) *Rc* between AIRS and CC from July 2006 to February 2011.

From the comparison of the original vertical distributions between CF and ECF (Figure 2a), both ECF (AIRS) and CF (CC) show a similar vertical distribution. Almost all clouds distribute below 13 km. The lower layers have large CF (ECF) values, and then they decrease as the height rises. The values of ECF are significantly lower than those of CF below 13 km. The peak of ECF is located around 2 km, while the peak of CF appears at a slightly lower height around 1 km. These differences may come from different detection capabilities between AIRS and CloudSat/CALIPSO. Figure 2b displays a comparison of the *Rc* vertical distribution between ECF/AIRS and CF/CC. Both of them show a relatively consistent vertical distribution with closer values. The peak height (about 2 km) of *Rc* of ECF/AIRS is also higher than that of CF/CC (about 1 km). In addition, the dispersion of AIRS (thin red lines) is more obvious than that of CC when converted into *Rc*, and both of them are more divergent at the peak height. After exceeding the peak, both of *Rc* begin to decrease with increasing height, and the difference between the two kinds of *Rc* also decreases. About 5 km or above, the two *Rcs* are close.

It should be noted that the definition of mid-level clouds differs to the observational methods. Mid-level clouds obtained through surface-based observation are typically defined as having a cloud top or base height between 3 and 8 km [13,34]. For satellite

observations, the most common definition of mid-level clouds comes from the International Satellite Cloud Climatology Project (ISCCP) [35]. Mid-level clouds are classified as the clouds with a cloud top pressure between 440 and 680 hPa [2,35,36]. According to the ISCCP standard, three layers that are 648, 548, and 447 hPa (corresponding to about 3.37, 4.59, and 6.02 km in Figure 2) are selected for analysis. Figure 3 shows the comparisons of the spatial distributions between monthly mean ECF (AIRS) and CF (CC) of mid-level clouds at three selected layers over the Arctic region (60°N to 82°N) during July 2006 to February 2011. It is noted that the spatial distribution patterns of them are highly consistent for selected layers, although the values are different. The maximum difference appears in Greenland. For AIRS, the area with higher ECF is concentrated in the nearshore coastal zone of Greenland, while CC observation shows that the area with higher CF is located in the south-central region of Greenland. According to Figure 2, AIRS has less capability to detect low-level clouds than CC under the condition of multi-layered clouds. The high geographical elevation of Greenland (Figure 1) might be one of the reasons causing the differences in cloudiness between AIRS and CC. Liu et al. [37] evaluated 16 available derived daytime CF products from satellite observations over the Arctic. They also found that Greenland has the greatest uncertainties, where the active satellite product tended to capture more clouds.
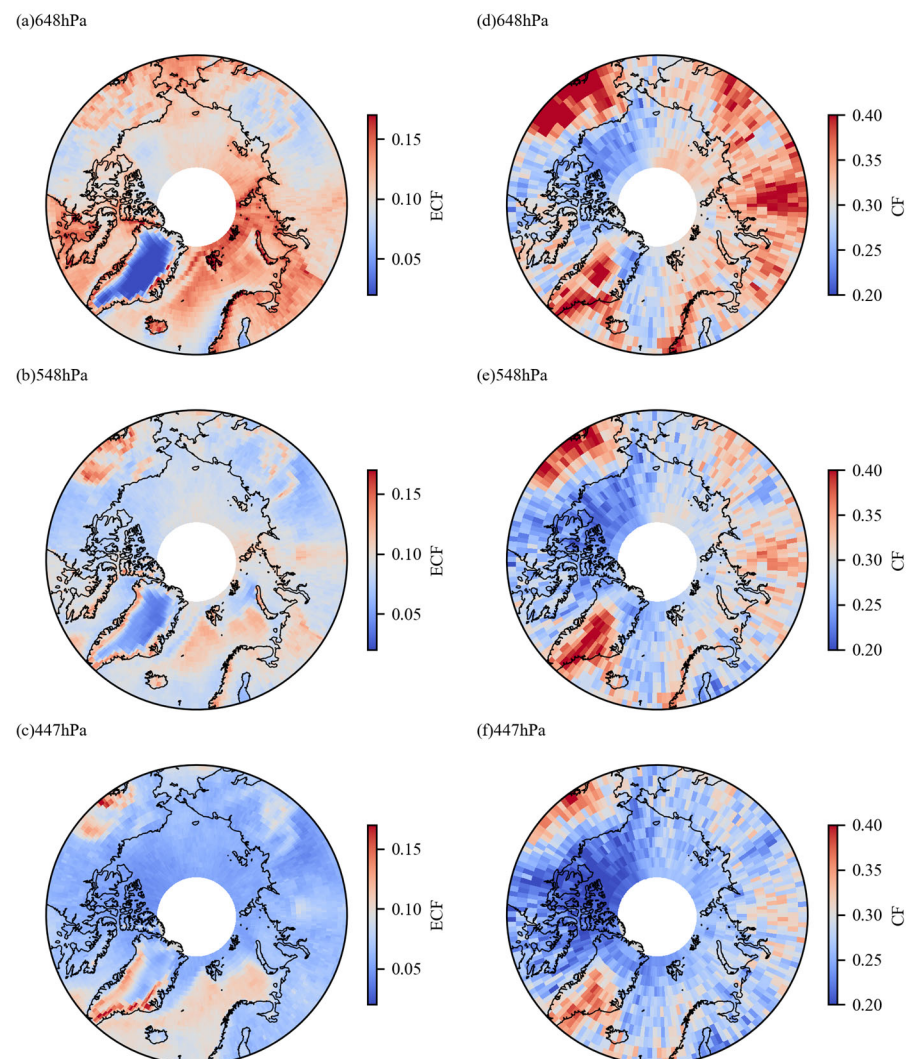

Figure 3. Comparisons of spatial distributions of monthly mean mid-level CF (ECF) between AIRS and CC over the Arctic region (60°N to 82°N) during July 2006 to February 2011. (**a**–**c**) Represent ECF of AIRS at 648, 548, and 447 hPa, respectively; (**d**–**f**) represent CF of CC at 648, 548, and 447 hPa, respectively.

According to the *Rc* seasonal variations (Figure 4), there are some differences between the ECF of AIRS and the CF of CC. For 648 hPa (blue lines), both ECF (solid line) and CF (dot line) peak in June. The most obvious difference occurs in May, when the CF shows a trough, while the ECF gradually increases. The variations in summer (June to August) are basically the same. For ECF, there is little change in autumn (September to November), while the CF shows a significant decrease in October. For CC, the monthly variations in *Rc* in the three layers are similar, but for AIRS, 548 and 447 hpa have an obvious increase from May to August. For 548 (green lines) and 447 hPa (cyan lines), the differences in ECF and CF are concentrated in early spring (March and April) and late summer (August). Generally, the ECF and CF both show their first trough in May. The CF peaks in July, while the ECF peaks are delayed until August. Both of them entered a second trough simultaneously in October. It should be noted that the months with larger differences between AIRS and CC always corresponded to larger standard deviations (STD) of CC, especially in early spring (with STD of 0.73 and 0.53 for 548 and 447 hPa in March and STD of 0.59 and 0.88 for 548 and 447 hPa in April). Liu et al. also proposed that the maximum difference between satellite daytime CF products occurred in April, when most passive satellite data underestimated CF [37]. This is consistent with our findings.
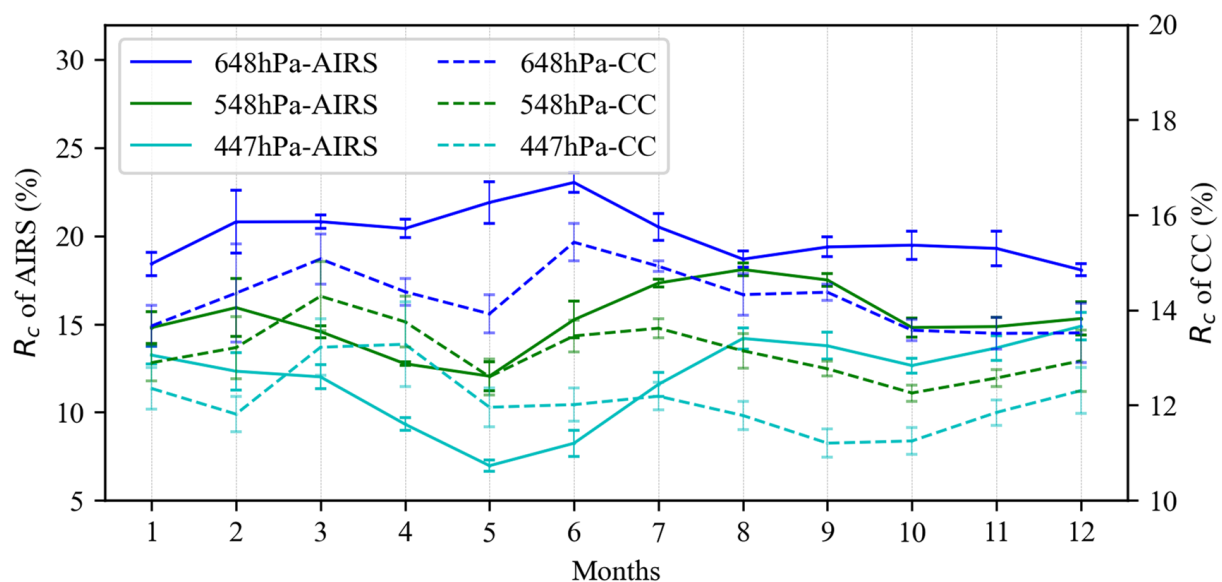

Figure 4. Seasonal variations in *Rc* at mid-level (648, 548, and 447 hPa) between AIRS and CC over the Arctic region (60°N to 82°N) during July 2006 to February 2011. The error bar represents the standard deviation of each month.

According to the above analysis, it is known that AIRS and CC have similar spatial and temporal distribution patterns, although they have different values.

2.2. Sea Ice Data

The Passive Microwave Sea Ice Concentration (version 3) product is applied here for sea ice concentration (SIC) analysis. It is a Climate Data Record (CDR) of SIC based on passive microwave observations, which is provided by NASA's National Snow and Ice Data Center (NSIDC) [38]. The biases are reported as +1.0~+3.5% during winter and +5~+10% during summer in the Arctic [39]. The SIC product is processed on a 25 × 25 km EASE grid. The SICs of September from 2003 to 2022 are used here for further analysis.

Sea ice leads represent elongated cracks covering up to hundreds of kilometers in length where open water and thin ice is present. Fabian Reiser et al. proposed a new algorithm to identify sea ice leads automatically by satellite thermal infrared images [40]. The output data provide daily sea ice lead maps [41] for cold seasons of November to April from 2002 to 2021, with a resolution of 1 km². The maps are classified into 6 categories

including clouds, land, sea ice, artefacts, leads, and open water [40]. For further analysis, here the daily maps were used to derive the leads numbers in November, with artefacts and clouds being excluded.

3. Results

3.1. Seasonal Variations of AIRS Mid-Level ECF

The percentages of ECF at different pressure layers to the total ECF for the AIRS ascending and descending orbits based on AIRS L3 monthly data from 2002 to 2022 are listed in Table 1. The proportion of low-layer cloud cover is relatively small, and the maximum cloud cover layer appears in 771 hPa. Below 771 hPa, the proportion of cloud cover decreases with the increasing pressure. For mid-level clouds (between 680 and 440 hPa, as defined in Section 2), the proportion to the total cloudiness is high, accounting for 47.56% (ascending orbit) and 48.66% (descending orbit), respectively. It also shows that the proportion of mid-level clouds to total cloud cover obtained by AIRS has no obvious diurnal characteristics.

Table 1. The percentage of ECF at each pressure layer to the total ECF for the AIRS for ascending and descending orbits.

Layers (hPa)	Percent of ECF (%)		Layers (hPa)	Percent of ECF (%)	
	Ascending	Descending		Ascending	Descending
1018	4.9822	5.8111	346	9.1497	9.6849
887	8.5849	8.0757	274	2.8735	3.1472
771	25.7638	23.1594	224	1.0029	1.1303
648	21.2827	21.3865	173	0.0838	0.1047
548	14.9392	15.5300	122	0.0003	0.0003
447	11.3360	11.9693	32	0.0003	0.0002

The monthly ECF variations and anomalies of three mid-levels (including 648, 548, and 447 hPa) from AIRS for both ascending and descending orbits from January 2003 to December 2022 are shown in Figure 5. Here, the ECF anomaly means the bias between the monthly ECF value and the multi-year average ECF for that month. The pink shadow represents positive bias and the blue shadow shows negative bias. The results reveal that the mid-level ECF values have significant seasonal variations. The high values of ECF in three mid-level layers occur in summer and the low values primarily occur in early spring. The ECF anomalies are notably larger at 648 hPa than those at 548 and 447 hPa. For the ECF at 648 hPa (Figure 5a,b), the seasonal extreme value generally displays a weakening trend. The maximum value of the warm seasons decreases gradually, and it is most significant during the periods of 2019–2020, when the ECF anomalies turn to negative values. The seasonal maximum in 2021 and 2022 have elevated again. For the minimum occurring in the cold seasons, the trend is more notable. The ECF anomalies of 648 hPa present significant positive values in the cold seasons since 2015. The ECF anomalies in the cold season of 2019 are up to more than 0.02, which is about 27% of the multi-year average ECF for that month. For the ECF of 548 hpa (Figure 5c,d) and 447 hPa (Figure 5e,f), it generally remained a relatively stable seasonal cycle, except for the periods of 2019–2020, when the seasonal maximum decreased, and for the periods of 2021 and 2022, when the maximum increased notably.

To further analyze the spatial differences of long-term ECF, the Arctic region is divided into six latitude zones (60–65°N, 65–70°N, 70–75°N, 75–80°N, 80–85°N, 85–90°N) and six meridional zones (180–120°W, 120–60°W, 60–0°W, 0–60°E, 60–120°E, 120–180°E), which are displayed in Figure 1.
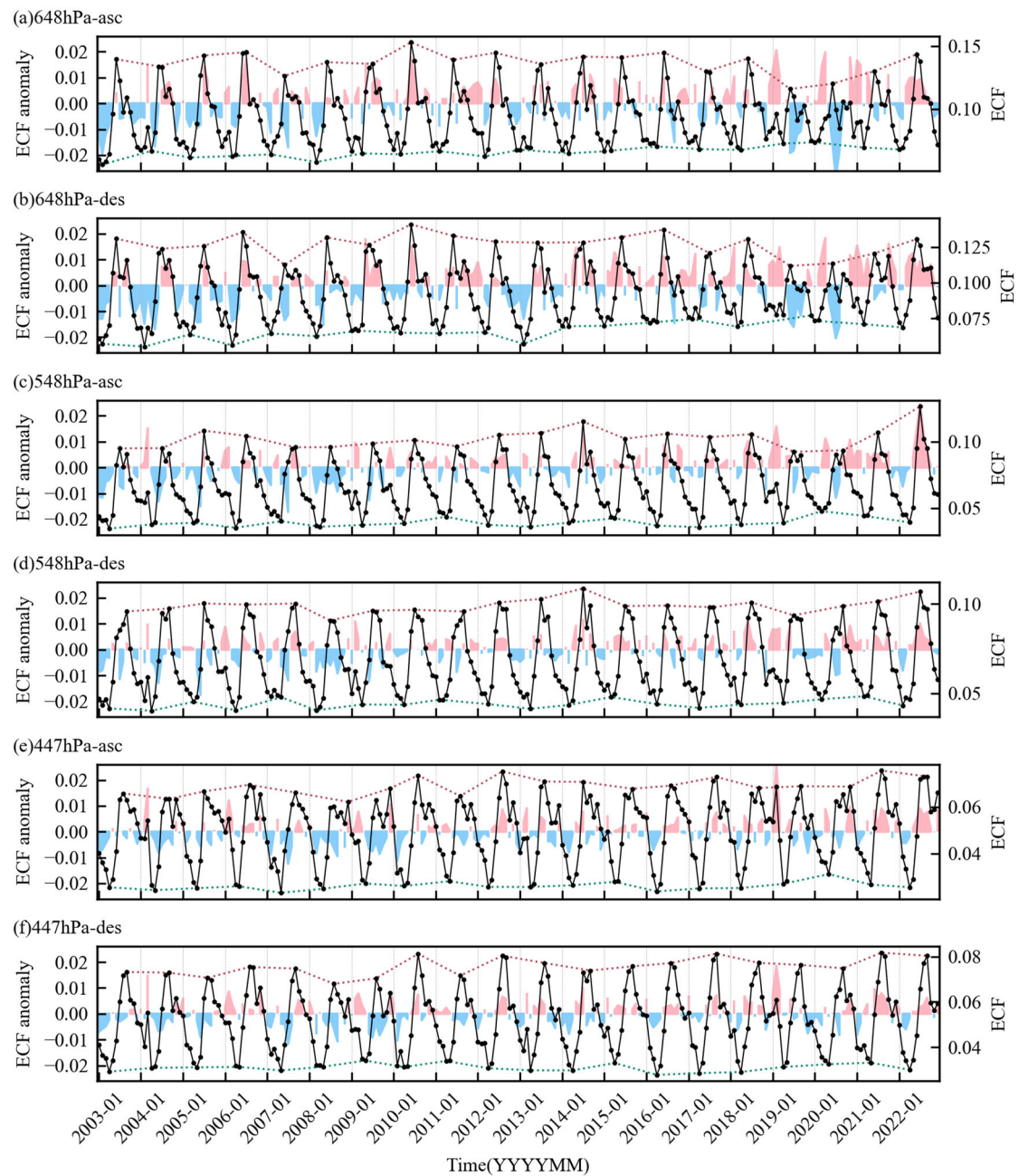
Figure 5. Monthly variations (dot-lines), anomalies (pink shadows for positive anomalies, blue shadows for negative anomalies), and extreme value envelopes (dotted lines) of AIRS mid-level ECF at (**a**,**b**) 648 hPa, (**c**,**d**) 548 hPa, and (**e**,**f**) 447 hPa for the ascending and descending orbits from January 2003 to December 2022.

The Hovmoller diagram is used here to show the ECF temporal variations in different spatial zones. Figure 6 demonstrates the monthly variations in AIRS mid-level ECF at 648 hPa, 548 hPa, and 447 hPa for the six defined Arctic latitude zones of both ascending and descending orbits from January 2003 to December 2022. Overall, the ECF increases with latitude in the above three pressure layers and basically maintains similar seasonal cycles between the ascending and descending orbits. From the perspective of intra-year variations, the ECF seasonal extremes at different pressure layers display notable differences among defined latitude zones. The ECF seasonal cycle of 648 hPa (Figure 6a,b) is dominated by a single peak within a year over the latitude zones north of 80°N. As the latitude decreases, it gradually changes to an obvious bimodal structure with significantly reduced peak values.

For 548 hPa (Figure 6c,d), except for the region north of 85°N, there is not much difference in the peak values among other latitude zones, but with decreasing latitude, the occurrence time of the peak is delayed. This delay phenomenon also occurs at 447 hPa (Figure 6e,f).
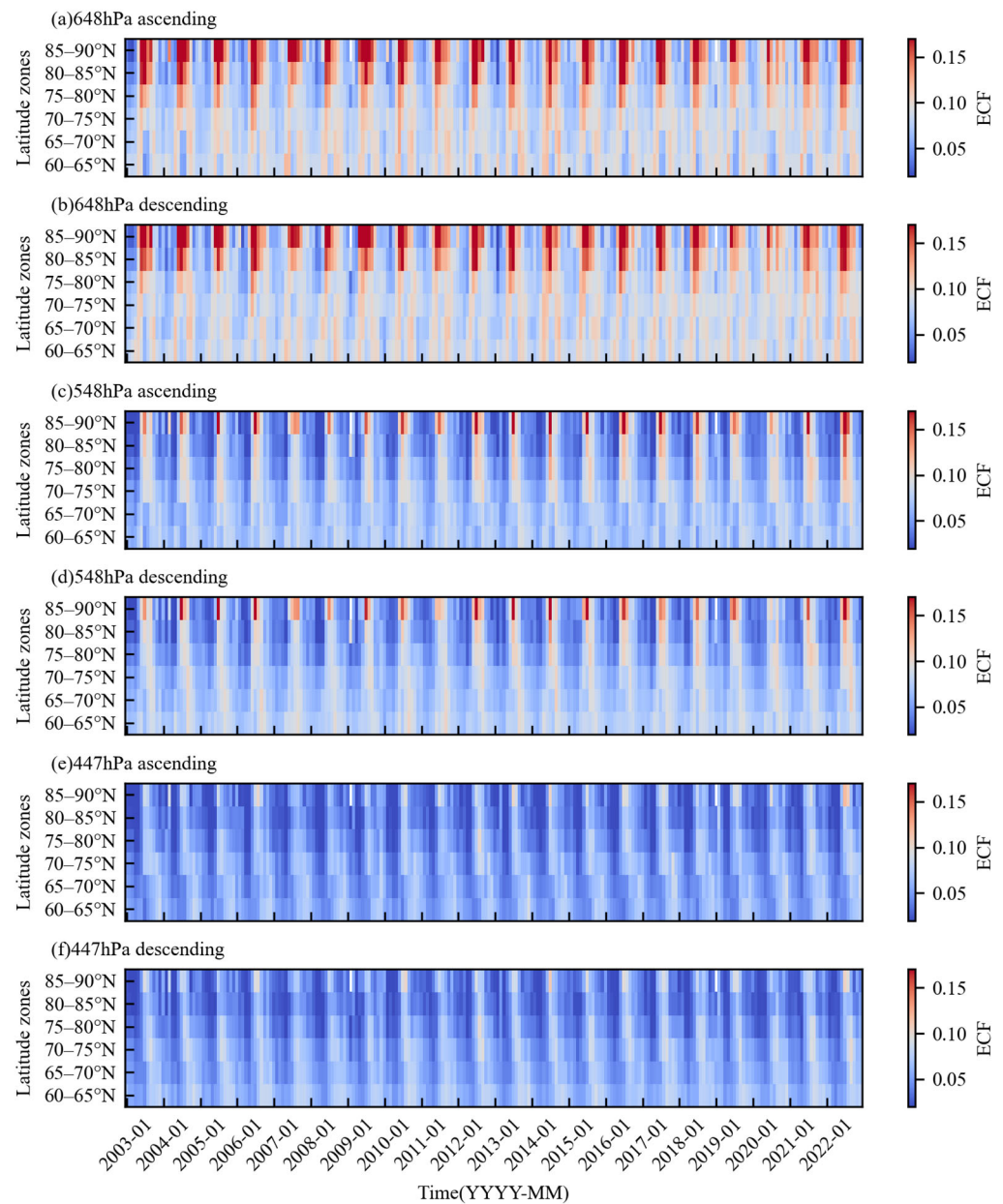

Figure 6. Monthly variations in AIRS ECF at mid-levels of (**a**,**b**) 648 hPa, (**c**,**d**) 548 hPa, and (**e**,**f**) 447 hPa for different Arctic latitude zones (60–65°N, 65–70°N, 70–75°N, 75–80°N, 80–85°N, 85–90°N) of ascending and descending orbits from January 2003 to December 2022.

The ECF value varies in different latitude zones. To further investigate the seasonal cycle trends of separate latitude zones, the coefficient of variation (CV) is introduced here. It is a standardized, unitless measure that is used for comparing variability between disparate groups and characteristics. The value of CV indicates the size of a standard deviation in relation to its mean, which is defined as (2):

$$c_v = \sigma/\mu,\qquad(2)$$

where σ represents the standard deviation; μ represents the mean value.

The CV values of mid-level ECF from AIRS for different Arctic latitude zones are displayed in Figure 7. Generally, the high-latitude zones have higher CV values compared to low-latitude zones. For the ECF at 648 hPa (Figure 7a,b), the values of CV show a clear decreasing trend for all the regions north of 80°N, both in ascending and descending orbits. The highest values of CV of the ascending orbits occurred in 2003, which are 0.683 (ascending) and 0.680 (descending) for the zone of 85–90°N, and 0.554 (ascending) and 0.513 (descending) for the zone of 80–85°N. The result indicates that the CV minimums appear in 2020 for the zone of 85–90°N (0.313 and 0.285 for ascending and descending orbits) and 2019 for the zone of 80–85°N (0.284 and 0.249 for ascending and descending orbits). The CV has increased again since 2021. The CV at 548 hPa (Figure 7c,d) and 447 hPa (Figure 7e,f) shows a significant decreasing trend during the period of 2003 to 2009 for the latitude zone of 85–90°N. Furthermore, they all demonstrate a prominent decrease in a single year since 2010. The CV for the region of 60–75°N is relatively stable, with lower values compared to the zones north of 75°N.
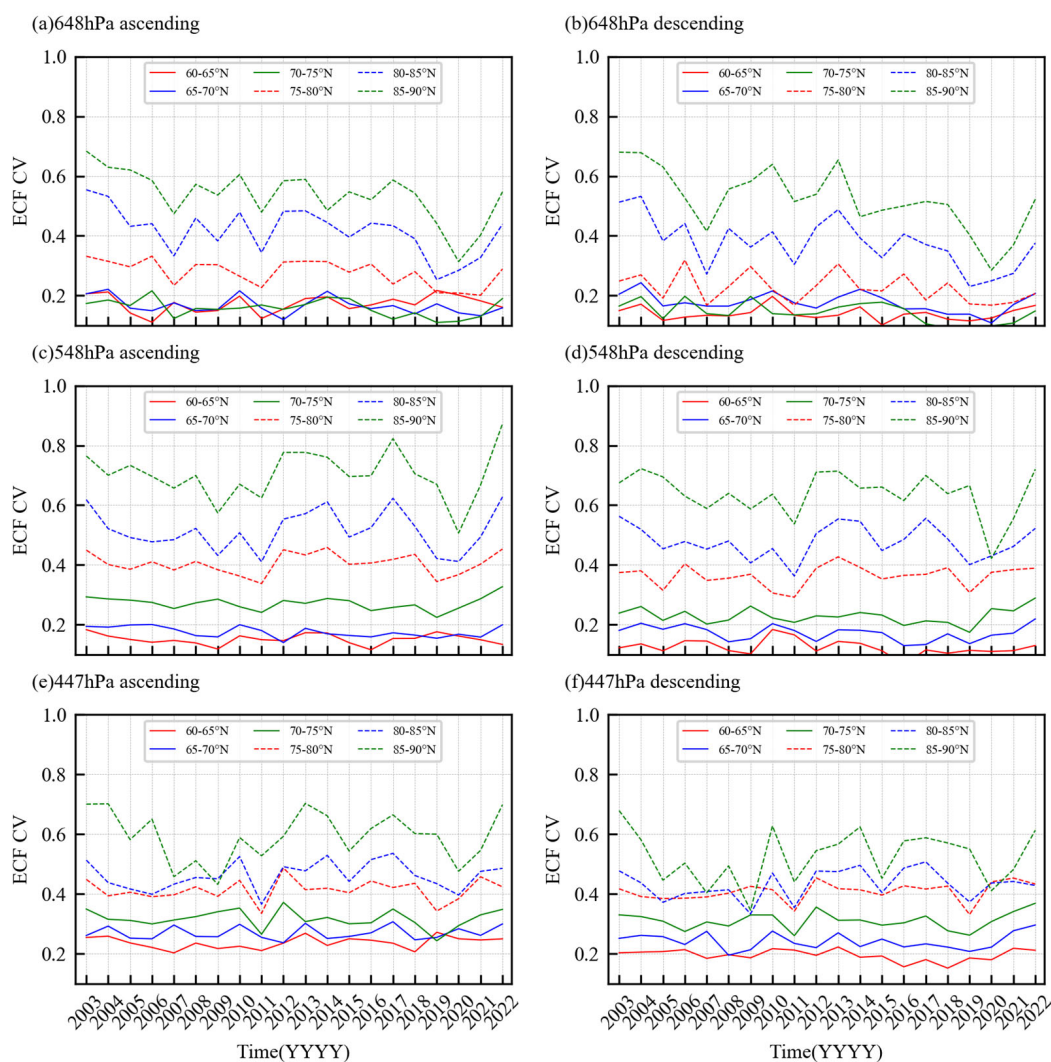

Figure 7. CV of AIRS ECF at mid-levels of (**a**,**b**) 648 hPa, (**c**,**d**) 548 hPa, and (**e**,**f**) 447 hPa for different Arctic latitude zones (60–65°N, 65–70°N, 70–75°N, 75–80°N, 80–85°N, 85–90°N) of ascending and descending orbits from 2003 to 2022.

Figure 8 shows the monthly variations in AIRS mid-level ECF at 648 hPa, 548 hPa and 447 hPa for the six defined Arctic meridional zones (180–120°W, 120–60°W, 60–0°W, 0–60°E, 60–120°E, 120–180°E) of both ascending and descending orbits from January 2003 to December 2022. For the meridional variations, there is no notable difference between

the ascending and descending orbits. Unlike the latitude zones, no significant advance or delay in the occurrence time for the ECF seasonal extreme was found among different meridional zones. The comparisons among the meridional zones reveal that the zones of 60–0°W and 0–60°E are quite distinct. As shown in Figure 1, the 60–0°W region is dominated by Greenland, while the 0–60°E region is mainly covered by sea areas with less sea ice coverage. The results indicate that the seasonal variations in mid-level ECF within these two zones are notably weaker than those of the other meridional zones. From the perspective of multi-year variations, the seasonal peak in the zone of 60–0°W has an obvious increasing trend, especially for the ECF at 548 hPa.
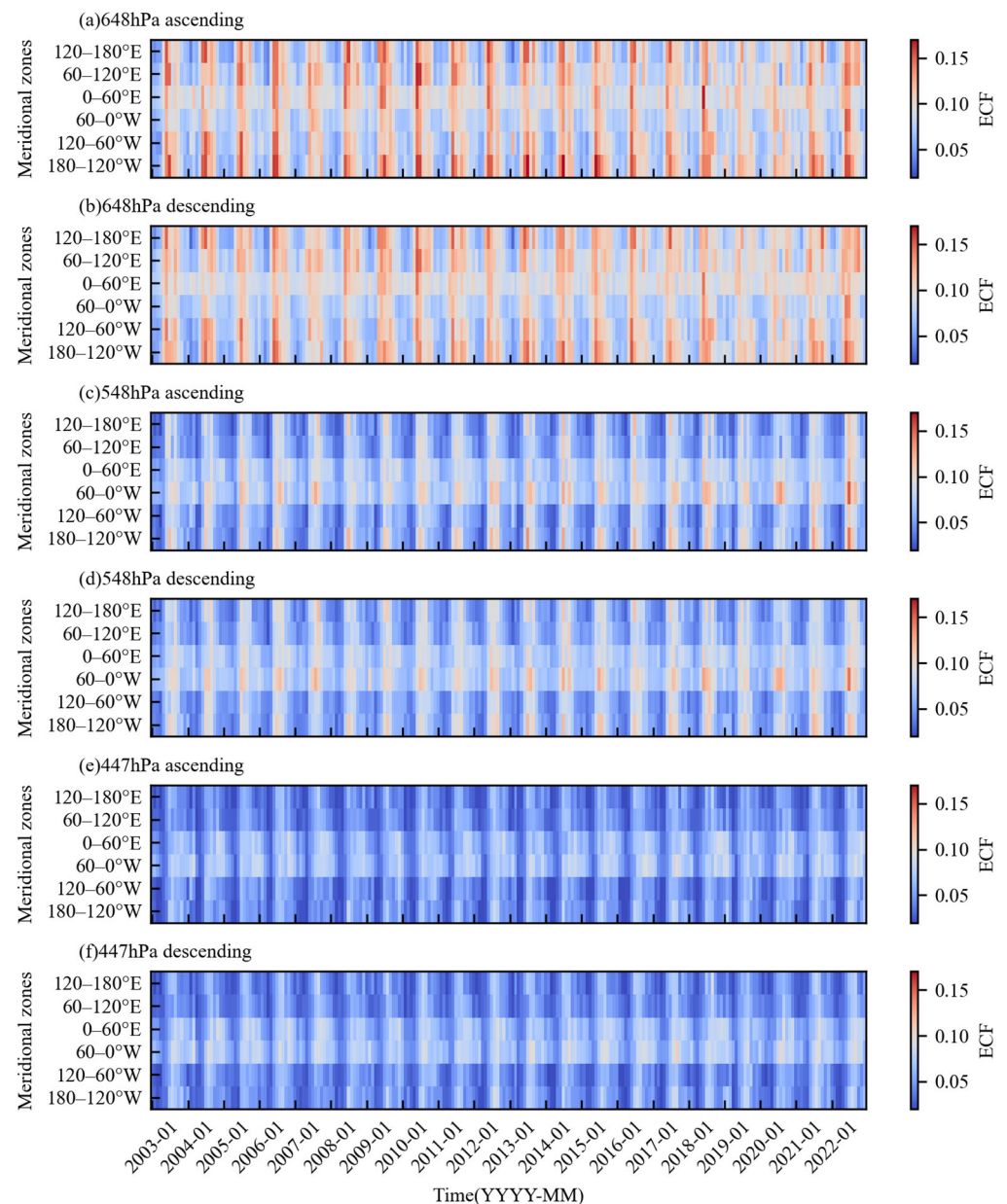

Figure 8. Monthly variations in AIRS ECF at mid-levels of (**a,b**) 648 hPa, (**c,d**) 548 hPa, and (**e,f**) 447 hPa for different Arctic meridional zones (180–120°W, 120–60°W, 60–0°W, 0–60°E, 60–120°E, 120–180°E) of ascending and descending orbits from January 2003 to December 2022.

The CV values of mid-level ECF from AIRS for different Arctic meridional zones are displayed in Figure 9. The results show that for the mid-level ECF (648 hPa, 548 hPa, and 447 hPa), the CV is relatively lower in the regions of 60–0°W and 0–60°E, indicating that the seasonal variation is relatively weaker than that in other regions, which is consistent with

the result from Figure 8. Similar to the zonal variations, the CV of 648 hPa (Figure 9a,b) also shows a relatively significant decreasing trend from 2003 to 2019 except for the zones of 60–0°W and 0–60°E. The CV began to increase in 2020. There is no obvious trend of CV at 548 hPa (Figure 7c,d) and 447 hPa (Figure 9e,f). In addition, the results show that the CV difference among different meridional zones gradually narrows as the pressure level elevates.
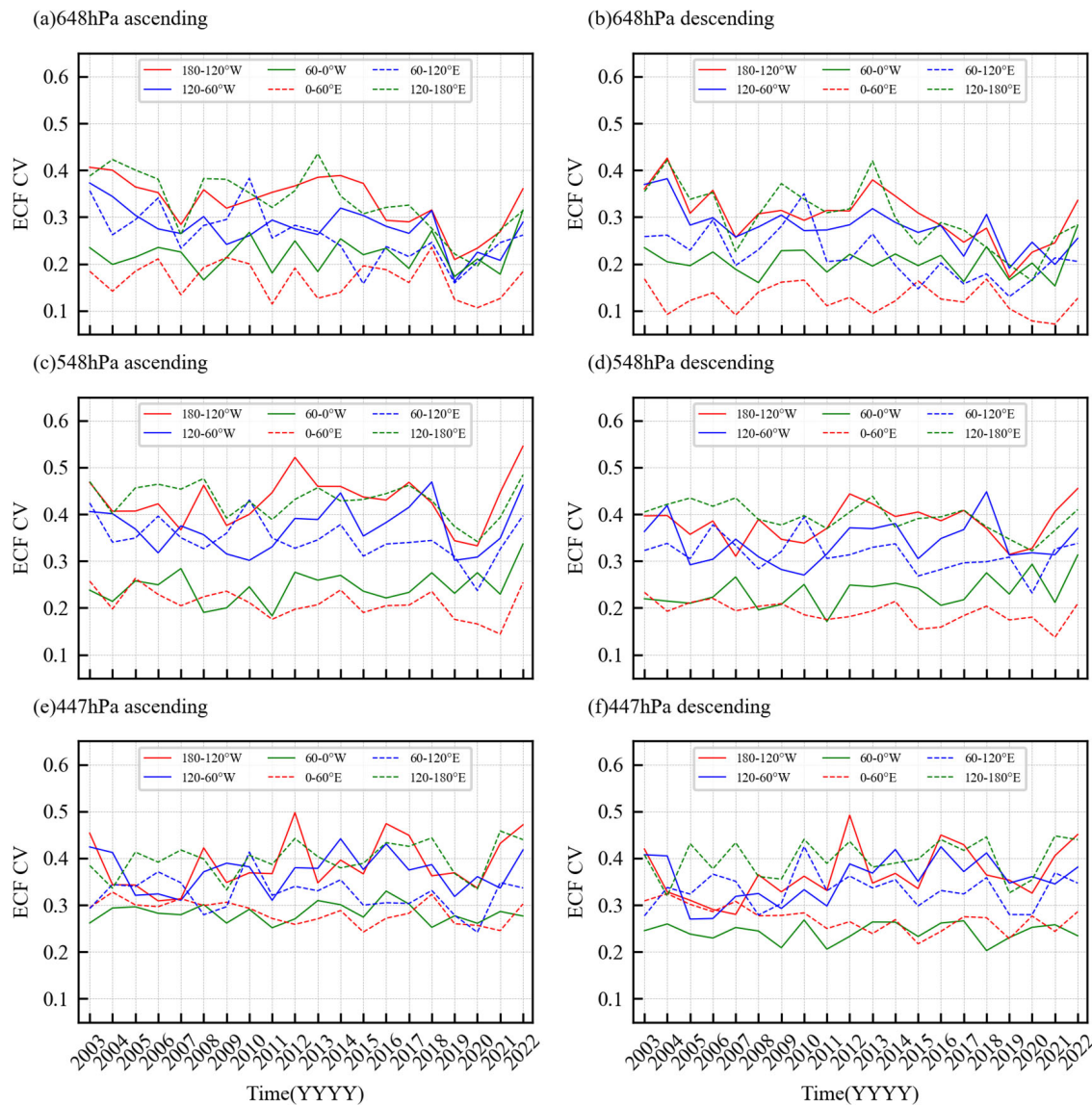

Figure 9. CV of AIRS ECF at mid-levels of (**a**,**b**) 648 hPa, (**c**,**d**) 548 hPa, and (**e**,**f**) 447 hPa for different Arctic meridional zones (180–120°W, 120–60°W, 60–0°W, 0–60°E, 60–120°E, 120–180°E) of ascending and descending orbits from 2003 to 2022.

3.2. Relationships between AIRS Mid-Level ECF and the Arctic Sea Ice

To further investigate the relationships between the seasonal cycle of the mid-level ECF and the Arctic sea ice, the SIC data from the NSIDC are selected here. Figure 10 displays the correlations between the CV of mid-level ECF from AIRS and the September SIC during 2003 to 2022. Note that the CV in Figure 10 is derived based on the mid-level ECF only over the sea regions of the Arctic (north of 60°N). In addition, in order to match the SIC of September (which is generally considered to be the minimum concentration of sea ice in the current year), the ECF from September of the previous year to August of the current year is used to generate the seasonal CV.
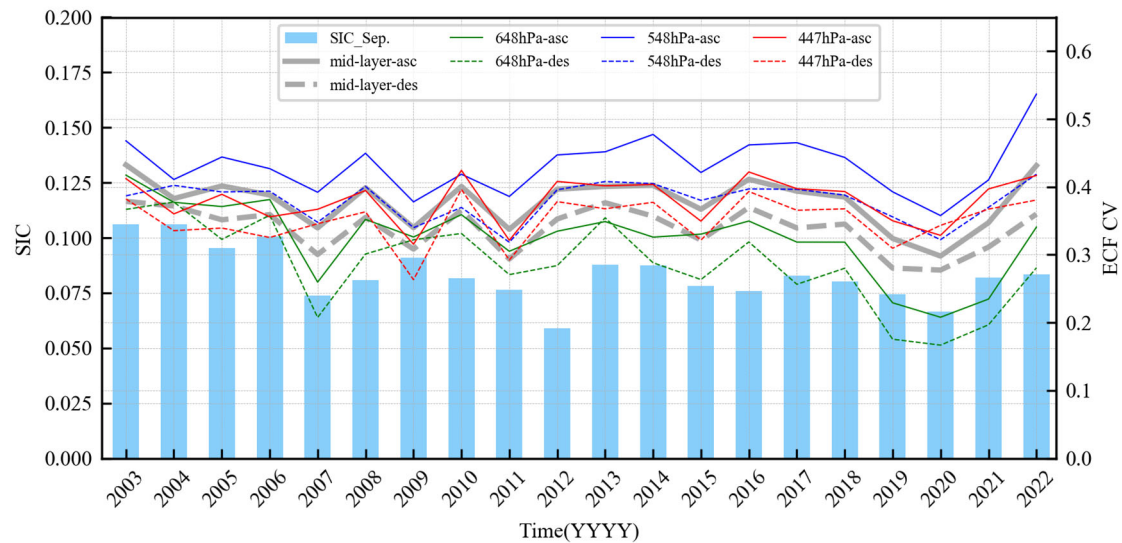
Figure 10. Correlations between the CV of AIRS ECF and the September SIC from 2003 to 2022 for the sea regions of the Arctic (north of 60°N). The thin solid and dotted lines represent the ECF CV at 648, 548, and 447 hPa of ascending and descending orbits, respectively. The thick gray solid and dashed lines represent the average CV of the mid-level ECF for the ascending and descending orbits, respectively. The blue bars represent the SIC in September of each year.

For each pressure layer, the CV variations are basically consistent between ascending (solid lines) and descending (dashed lines) orbits. Moreover, the CV value of the descending orbit is slightly lower than that of the ascending one. When the pressure layer varies, the trend of CV is slightly different. Compared with 648 and 447 hpa, the CV at 548 hpa is notably higher. Generally, the result reveals that the decrease in the seasonal mean CV of mid-level ECF (gray solid and dashed lines) essentially corresponds to the retreat of sea ice in September in Arctic. The valley values of the seasonal mean CV vary primarily in phase with the years of exceptionally low September SIC over the past two decades, notably in 2007 and the most recent occurrence in 2020. However, for the lowest SIC record observed in 2012, the seasonal mean CV of mid-level clouds presented a rising trend. It is worth mentioning that the seasonal mean CV experienced a significant decline, reaching a low point in 2011, which occurred a year prior to the extreme sea ice low event in 2012. Research has consistently focused on understanding the causes behind the extreme retreat of sea ice in 2012. Some pointed out that the strong storm that entered the central Arctic in early August 2012 accelerated the decline of the Arctic sea ice [42,43]. According to a recent study [44], the occurrence of back-to-back La Niña events in 2010–2011, along with subsequent North Pacific cooling and a marginal El Niño, played a significant role in contributing to the low SIC record in 2012. The sharp decline in the seasonal CV of mid-level clouds here might present an additional potential early indicator of the occurrence of extreme low sea ice events, although further research is needed to fully understand its mechanisms.

Singular value decomposition (SVD) is always used for pairwise analysis of data fields by examining their variations over time, as indicated by the SVD time series [45,46]. Here, the SVD analyses are conducted to investigate the potential covariability characteristics between the seasonal cycle of the mid-level ECF and the Arctic sea ice. Instead of the SIC, the leads data are employed here, which could provide more detailed variations in sea ice at spatial scales. The total leads numbers in November are calculated in the gird cells of AIRS. The time period is from 2003 to 2021. It is noted that to match the leads in November, the ECF from November of the previous year to October of the current year is used to generate the seasonal CV. Here, the left field is the CV anomaly, and the right field is the leads anomaly.

Figure 11 shows the first four SVD modes (total explained covariance: 38.87%) for the CV anomalies of AIRS mid-level ECF (ascending orbits) and leads numbers anomalies in November. The first SVD mode (SVD1) explains 14.78% of the total squared covariance. The spatial patterns of SVD1 heterogeneous correlations reveal a relatively strong coupling in the central Arctic Ocean (Figure 11a,b), featuring large areas with positive CV anomalies and negative leads anomalies. Only the regions north of the Canadian Arctic Archipelago are characterized by positive anomalies for both CV and leads. For the Kara and Barents Seas, SVD1 also indicates positive anomalies in CV and leads. The time series of the left and right fields of SVD1 (Figure 11c) vary generally in phase, with a correlation coefficient of 0.81, indicating a close linkage between CV and leads.
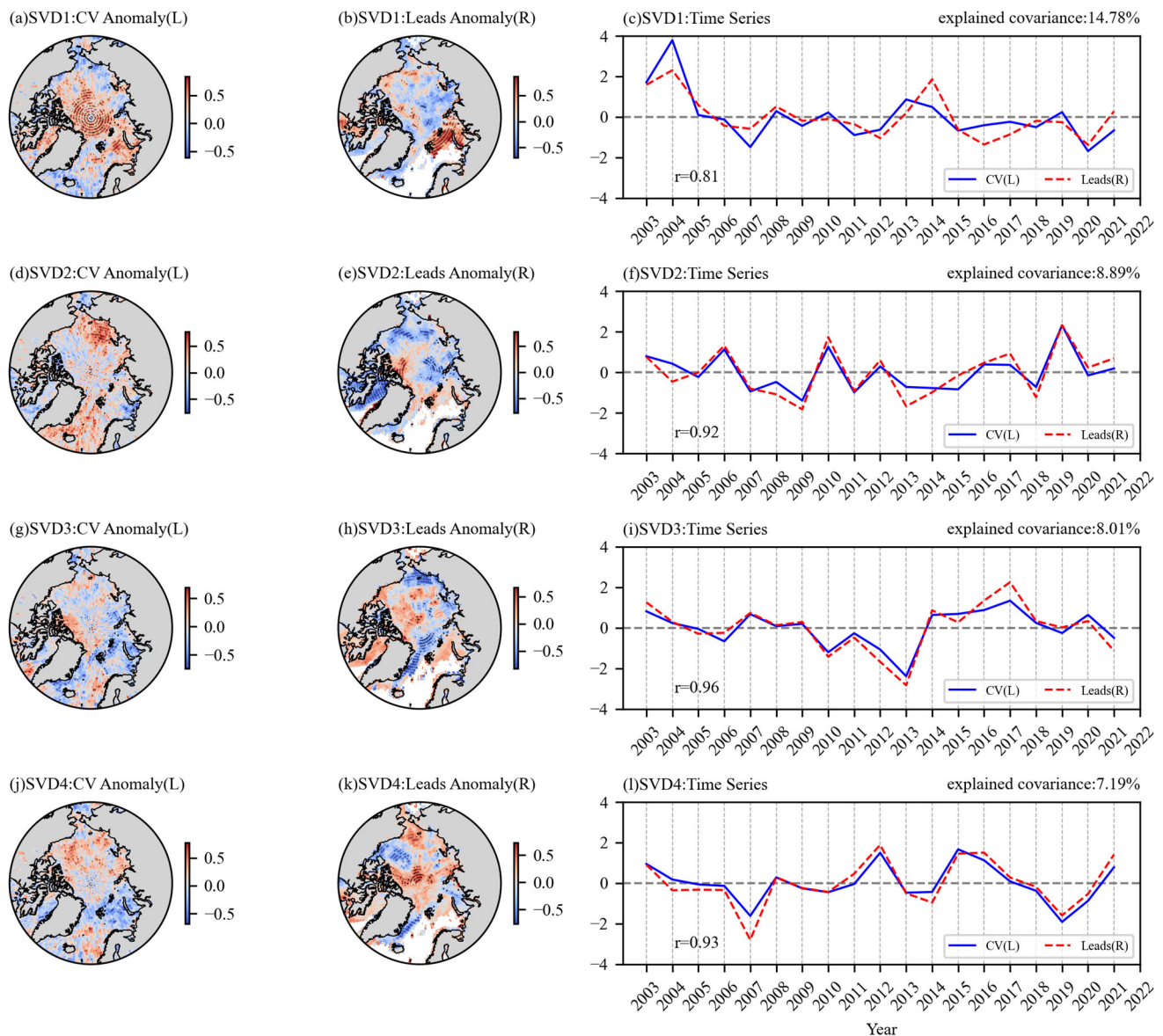

Figure 11. (**a,b,d,e,g,h,j,k**) Spatial patterns of the heterogeneous correlations and (**c,f,i,l**) time series of the left and right fields of the SVD1 to SVD4 modes for the CV of AIRS mid-level ECF (ascending orbits) and leads numbers in November in the Arctic. L represents left field; R represents right field. The dotted area in panels (**a,b,d,e,g,h,j,k**) indicates correlations passing the 95% statistical significance level.

The SVD2 to SVD4 modes account for 24.09% of the total squared covariance. Generally, the spatial patterns suggest reverse anomalies for most regions of the central Arctic.

The correlation coefficients of the time series of SVD2 to SVD4 are about 0.92, 0.96, and 0.93, respectively. As in Figure 11, Figure 12 displays the situations of the descending orbits. The total explained covariance is 39.39%, with the first mode accounting for about 15.05%. The spatial patterns of SVD modes are nearly consistent with the ones of the ascending orbits, except SVD2. The main differences are concentrated north of the Bering Strait, featuring negative CV anomalies and positive leads anomalies. The correlation coefficient of the time series of SVD2 for the descending orbits is 0.96, which is higher than that for the ascending orbits, suggesting that the relationships between Arctic cloud and sea ice exhibit diurnal variation characteristics that warrant further study.
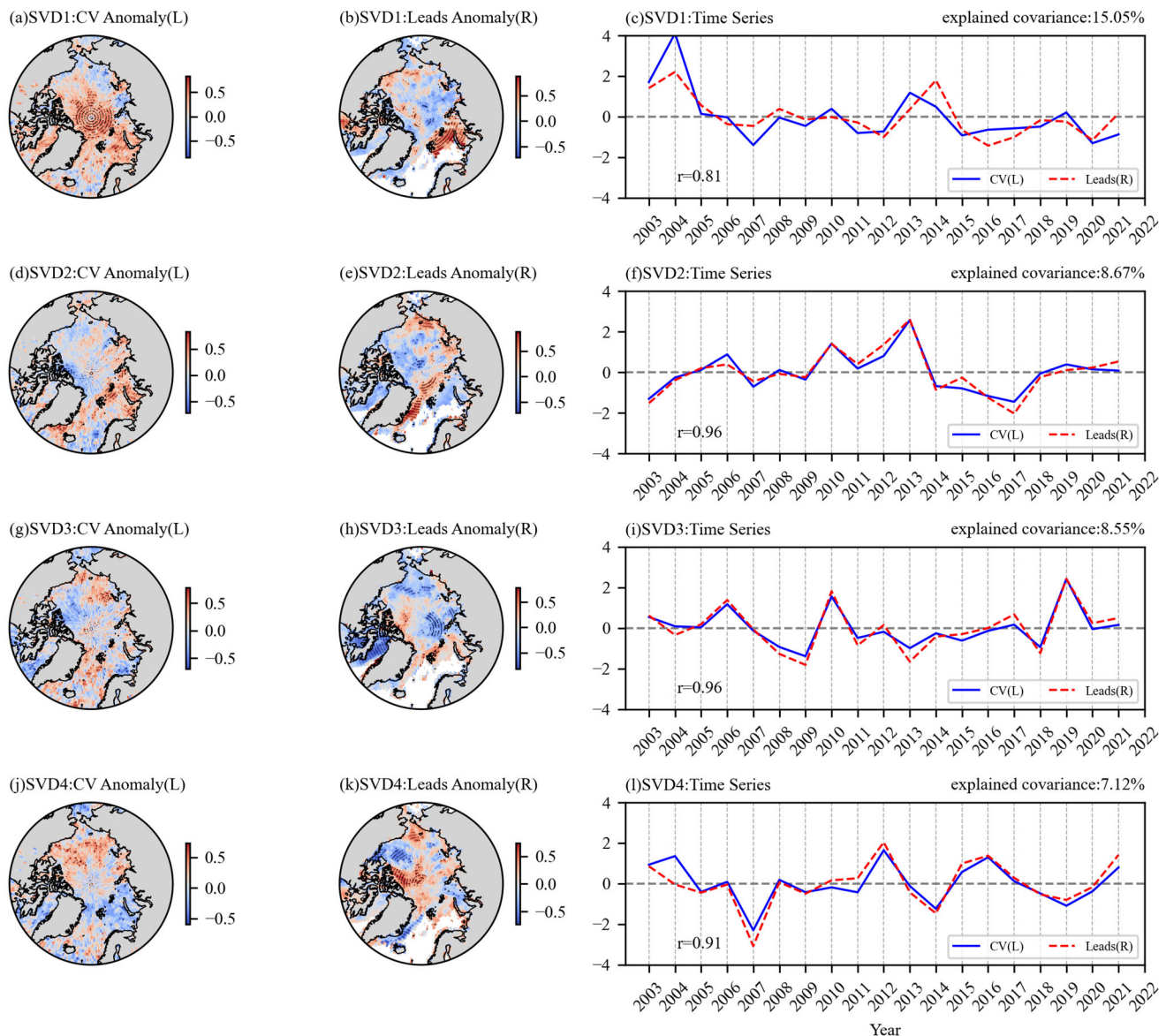
Figure 12. As in Figure 11, but for descending orbits.

The reverse anomaly spatial pattern, characterized by a positive (negative) CV anomaly corresponding to a negative (positive) leads anomaly, suggests a linkage between seasonal variations in mid-level clouds and sea ice retreat. This is consistent with the findings in Figure 10. Yet, this pattern appears to be regionally dependent. In the Greenland Sea and the areas near the Canadian Arctic Archipelago, both CV and leads show negative (positive) anomalies in SVD2 to SVD4 modes. The complex mechanism of sea ice variability in these areas has always been a difficult focal point of research. Recently, Chatterjee et al. [47]

highlighted that the combined influence of large-scale atmospheric and oceanic circulations in the Nordic Seas could explain the variability of sea ice in the Greenland Sea. Li et al. [48] also emphasized that sea ice floes are prevalent in the Greenland Sea influenced by drifting sea ice through the Fram Strait. The region near the Canadian Arctic Archipelago was another area pointed out, where both the sea ice and atmosphere were heavily influenced by the presence of land. Here, the spatial patterns in these areas present unique covariability characteristics between the CV of mid-level clouds and leads unlike most regions in the Arctic, further confirming that the sea ice variations in these regions are notably complex. In the future, it is essential to pursue more precise observations and advanced methods to study the intricate connections between clouds and sea ice by isolating other influencing factors more effectively.

4. Discussion

Here, the satellite observations are primarily from AIRS, which is a hyperspectral infrared atmospheric sounder with 2378 spectral channels ranging from 3.75 to 15.4 μm [22,49]. It obtains the atmospheric parameters corresponding to a range of heights through the sensitivity of channels to different atmospheric constituents. Benefiting from the AIRS's ability to make vertical observations, mid-level clouds and the related trends could be obtained and analyzed here. However, limited by the instrument performance and the analyzing method, there are still some issues that need to be noted and discussed as follows:

(1) The AIRS L3 standard product contains gridded retrieved parameters on the standard pressure levels roughly matching instrument vertical resolution. As we mentioned in Section 2.1, the effective cloud fractions are provided at 12 pressure layers. Clouds of only three pressure layers (648, 548, and 447 hPa) could be used to demonstrate the variations in mid-level clouds in the Arctic. Due to the numbers of discrete pressure levels, it may have certain limitations in capturing the fine-structured features of the mid-level clouds. However, through the preliminary comparisons with CC vertical clouds, which have a vertical resolution of 480 m, it reveals that AIRS vertical clouds above 2 km could basically represent the vertical distributions of clouds in the Arctic. Moreover, the spatial distribution of mid-level clouds is highly consistent with CC except for the controversial Greenland. Therefore, it suggests that AIRS vertical cloud fraction has the ability to represent the seasonal and annual cycle, and is useful in climatological anomaly studies, especially for the Arctic region, where persistent large-scale vertical observations for clouds are very rare.

(2) The cloud fraction used here is the ECF, a combination of cloud fraction and cloud emissivity, which is retrieved under the assumption that the cloud emissivity is spectrally flat [20]. It is retrieved by comparing observed AIRS radiance and calculated ones of channels sensitive to cloud amount and height, after cloud-clearing steps [50]. ECF has some differences to what is commonly referred to as cloud fraction. Therefore, for comparison, ECF from AIRS and CF from CC were normalized by calculating the proportion of each layer's ECF or CF to the total ECF or CF (accumulated over all vertical layers), in order to make the validation more reasonable. It should be noted that the original ECF is directly adopted in the follow-up analysis. On the one hand, in order to prevent the introduction of additional errors, on the other hand, preliminary validation reveals that the ECF could also characterize the variations in cloud amount, which is useful in climatological studies.

(3) There are certain differences in the definition of mid-level clouds in previous studies with different regions, seasons, and observation instruments. The definition of mid-level clouds used here comes from ISCCP, which considers cloud top pressure between 440 and 680 hpa. Meanwhile, American standard atmospheric profiles for Arctic summer and winter are employed here to convert between pressure and altitude. It is found that when using the summer and winter Arctic standard atmospheric profiles for pressure to height conversion of the middle layers (648, 548, and 447 hpa), the altitude is higher in summer than that in winter, with a difference of about 0.2 to

0.4 km. For comparisons with CC, the average summer and winter Arctic profile is applied here to perform the pressure and height conversion, which is relatively more accurate for representing the multi-year average state. In addition, it should be noted that for the clouds at 648 hpa of AIRS, their upper and lower boundary layers are 600 and 700 hpa, respectively. This indicates that 648 hpa actually contains parts of the low-level clouds, which may introduce certain analysis errors.

(4) When analyzing the correlations between seasonal variations in mid-level clouds and sea ice, the results obtained only based on the satellite observations used in this study may have some limitations. It has been demonstrated that changes in Arctic sea ice are influenced by various factors involved in complex mechanisms. Clouds impact the formations and variations of sea ice through their influence on radiation and related feedback mechanisms. Apart from clouds, atmospheric and oceanic circulation, as well as the coupling interactions, are also crucial factors in evaluating sea ice changes. To accurately assess the connection between clouds and sea ice, it is essential to isolate clouds from other influencing elements. This can be achieved by introducing more comprehensive and precise observational data and employing a more rational and advanced approach. In this study, our primary focus is on examining the long-term seasonal changes in Arctic mid-level clouds and conducting an initial analysis of the potential linkage between these changes and sea ice. Further in-depth research is warranted to investigate the mechanisms.

5. Conclusions

From the perspective of satellite observations, this study attempts to analyze the seasonal variations in mid-level clouds in the Arctic region over the past two decades and explore the possible relationships with sea ice changes. A comparative analysis of AIRS mid-level ECF by CC vertical CF is present, which indicates the availability of AIRS mid-level ECF for long-term climate analysis.

The results show that long-term diurnal variation in the Arctic mid-level clouds reflected by the ascending and descending orbits of AIRS is nearly consistent. For the mid-level clouds of three layers (648, 548, and 447 hPa) involved in AIRS data, the high values of ECF occur in summer and the low values primarily occur in early spring, while the seasonal variations are obviously different. The ECF anomalies are notably larger at 648 hPa than those at 548 and 447 hPa. Meanwhile, the ECF values at 648 hPa show a clear decreasing trend in seasonal CV for all the regions north of 80°N, which have their minimum CV during 2019 to 2020. Moreover, the seasonal CV of all these three layers is relatively lower in the regions of 60–0°W and 0–60°E, where the regions are dominated by Greenland and the sea areas with less sea ice coverage.

Our findings reveal that the decrease in the seasonal mean CV of mid-level ECF essentially corresponds to the retreat of Arctic sea ice in September. The seasonal CV anomaly of mid-level clouds and leads anomaly exhibit a reverse spatial pattern in the SVD analysis. However, this pattern appears to be regionally dependent. While in the Greenland Sea and the areas near the Canadian Arctic Archipelago, where the sea ice may be more influenced by atmospheric and oceanic circulations or the presence of land, both CV and leads show negative (positive) anomalies. In order to further evaluate the mechanisms between seasonal variations in mid-level clouds and sea ice, it is essential to isolate clouds from other influencing factors by introducing more comprehensive and precise data and employing more advanced approaches in the future.

References

1. Spänkuch, D.; Hellmuth, O.; Görsdorf, U. What Is a Cloud? Toward a More Precise Definition. *Bull. Am. Meteorol. Soc.* **2022**, *103*, E1894–E1929. [CrossRef]
2. Stubenrauch, C.J.; Chédin, A.; Rädel, G.; Scott, N.A.; Serrar, S. Cloud Properties and Their Seasonal and Diurnal Variability from TOVS Path-B. *J. Clim.* **2006**, *19*, 5531–5553. [CrossRef]
3. Sutphin, A.B. Characteristics of Tropical Midlevel Clouds Using A-Train Measurements. Master's Thesis, Texas A&M University, Bizzell, TX, USA, 2013.
4. Jin, H. Satellite Remote Sensing of Mid-Level Clouds. Doctoral Dissertation, Texas A&M University, Bizzell, TX, USA, 2012.
5. Rossow, W.B.; Zhang, Y. Evaluation of a Statistical Model of Cloud Vertical Structure Using Combined CloudSat and CALIPSO Cloud Layer Profiles. *J. Clim.* **2010**, *23*, 6641–6653. [CrossRef]
6. Zhang, D.; Wang, Z.; Liu, D. A global view of midlevel liquid-layer topped stratiform cloud distribution and phase partition from CALIPSO and CloudSat measurements. *J. Geophys. Res.* **2010**, *115*, D00H13. [CrossRef]
7. Hobbs, P.V.; Rangno, A.L. Microstructures of low and middle-level clouds over the Beaufort Sea. *Q. J. R. Meteorol. Soc.* **1998**, *124*, 2035–2071. [CrossRef]
8. Intrieri, J.M.; Shupe, M.D.; Uttal, T.; McCarty, B.J. An annual cycle of Arctic cloud characteristics observed by radar and lidar at SHEBA. *J. Geophys. Res. Ocean.* **2002**, *107*, SHE 5-1–SHE 5-15. [CrossRef]
9. Shupe, M.D.; Walden, V.P.; Eloranta, E.; Uttal, T.; Campbell, J.R.; Starkweather, S.M.; Shiobara, M. Clouds at Arctic Atmospheric Observatories. Part I: Occurrence and Macrophysical Properties. *J. Appl. Meteorol. Climatol.* **2011**, *50*, 626–644. [CrossRef]
10. Shupe, M.D. Clouds at Arctic Atmospheric Observatories. Part II: Thermodynamic Phase Characteristics. *J. Appl. Meteorol. Climatol.* **2011**, *50*, 645–661. [CrossRef]
11. Yan, Y.; Liu, X.; Liu, Y.; Lu, J. Comparison of mixed-phase clouds over the Arctic and the Tibetan Plateau: Seasonality and vertical structure of cloud radiative effects. *Clim. Dyn.* **2020**, *54*, 4811–4822. [CrossRef]
12. Achtert, P.; O'Connor, E.J.; Brooks, I.M.; Sotiropoulou, G.; Shupe, M.D.; Pospichal, B.; Brooks, B.J.; Tjernström, M. Properties of Arctic liquid and mixed-phase clouds from shipborne Cloudnet observations during ACSE 2014. *Atmos. Chem. Phys.* **2020**, *20*, 14983–15002. [CrossRef]
13. Riihimaki, L.D.; McFarlane, S.A.; Comstock, J.M. Climatology and Formation of Tropical Midlevel Clouds at the Darwin ARM Site. *J. Clim.* **2012**, *25*, 6835–6850. [CrossRef]
14. Adebiyi, A.A.; Zuidema, P.; Chang, I.; Burton, S.P.; Cairns, B. Mid-level clouds are frequent above the southeast Atlantic stratocumulus clouds. *Atmos. Chem. Phys.* **2020**, *20*, 11025–11043. [CrossRef]
15. Fleishauer, R.P.; Larson, V.E.; Vonder Haar, T.H. Observed Microphysical Structure of Midlevel, Mixed-Phase Clouds. *J. Atmos. Sci.* **2002**, *59*, 1779–1804. [CrossRef]
16. Bourgeois, Q.; Ekman, A.M.L.; Igel, M.R.; Krejci, R. Ubiquity and impact of thin mid-level clouds in the tropics. *Nat. Commun.* **2016**, *7*, 12432. [CrossRef] [PubMed]
17. Mantsis, D.F.; Sherwood, S.; Dixit, V.; Morrison, H.; Thompson, G. Mid-level clouds over the Sahara in a convection-permitting regional model. *Clim. Dyn.* **2020**, *54*, 3425–3439. [CrossRef]
18. Bourgeois, E.; Bouniol, D.; Couvreux, F.; Guichard, F.; Marsham, J.H.; Garcia-Carreras, L.; Birch, C.E.; Parker, D.J. Characteristics of mid-level clouds over West Africa. *Q. J. R. Meteorol. Soc.* **2018**, *144*, 426–442. [CrossRef]
19. Lacour, A.; Chepfer, H.; Shupe, M.D.; Miller, N.B.; Noel, V.; Kay, J.; Turner, D.D.; Guzman, R. Greenland Clouds Observed in CALIPSO-GOCCP: Comparison with Ground-Based Summit Observations. *J. Clim.* **2017**, *30*, 6065–6083. [CrossRef]
20. Kahn, B.H.; Irion, F.W.; Dang, V.T.; Manning, E.M.; Nasiri, S.L.; Naud, C.M.; Blaisdell, J.M.; Schreier, M.M.; Yue, Q.; Bowman, K.W.; et al. The Atmospheric Infrared Sounder version 6 cloud products. *Atmos. Chem. Phys.* **2014**, *14*, 399–426. [CrossRef]
21. Susskind, J.; Barnet, C.D.; Blaisdell, J.M. Retrieval of atmospheric and surface parameters from AIRS/AMSU/HSB data in the presence of clouds. *IEEE Trans. Geosci. Remote Sens.* **2003**, *41*, 390–409. [CrossRef]
22. Le Marshall, J.; Jung, J.; Derber, J.; Chahine, M.; Treadon, R.; Lord, S.J.; Goldberg, M.; Wolf, W.; Liu, H.C.; Joiner, J.; et al. Improving Global Analysis and Forecasting with AIRS. *Bull. Am. Meteorol. Soc.* **2006**, *87*, 891–895. [CrossRef]

23. Smith, N.; Barnet, C.D. CLIMCAPS observing capability for temperature, moisture, and trace gases from AIRS/AMSU and CrIS/ATMS. *Atmos. Meas. Tech.* **2020**, *13*, 4437–4459. [CrossRef]

24. Devasthale, A.; Sedlar, J.; Kahn, B.H.; Tjernström, M.; Fetzer, E.J.; Tian, B.; Teixeira, J.; Pagano, T.S. A Decade of Spaceborne Observations of the Arctic Atmosphere: Novel Insights from NASA's AIRS Instrument. *Bull. Am. Meteorol. Soc.* **2016**, *97*, 2163–2176. [CrossRef]

25. Chang, L.; Feng, G.; Zhang, Y.; He, X. Effect of Cloud Fraction on Arctic Low-Level Temperature Inversions in AIRS Observations Over Both Land and Ocean. *IEEE Trans. Geosci. Remote Sens.* **2018**, *56*, 2025–2032. [CrossRef]

26. Chang, L.; Chen, F.; Gao, G.; Zhang, Y. Effects of Water Vapor and Cloud Fraction in AIRS Retrievals on Arctic Sea Ice Variability. *IEEE Trans. Geosci. Remote Sens.* **2022**, *60*, 1–12. [CrossRef]

27. Tian, B.; Manning, E.; Roman, J.; Thrastarson, H.; Fetzer, E.; Monarrez, R. AIRS Version 7 Level 3 Product User Guide. Available online: https://docserver.gesdisc.eosdis.nasa.gov/public/project/AIRS/V7_L3_Product_User_Guide.pdf (accessed on 18 December 2023).

28. Susskind, J.; Blaisdell, J.; Iredell, L.; Lee, J.; Milstein, A.; Barnet, C.; Fishbein, E.; Manning, E.; Strow, L.; Teixeira, J. Algorithm Theoretical Basis Document-Airs-Team Retrieval for Core Products and Geophysical Parameters: Versions 6 and 7 Level 2. Available online: https://docserver.gesdisc.eosdis.nasa.gov/public/project/AIRS/L2_ATBD.pdf (accessed on 18 December 2023).

29. Manning, E.; Kahn, B.; Fetzer, E.J.; Yue, Q.; Wong, S.; Kalmus, P.; Payne, V.; Wang, T.; Olsen, E.T.; Wilson, R.C.; et al. AIRS/AMSU/HSB Version 7 Level 2 Product User Guide. Available online: https://docserver.gesdisc.eosdis.nasa.gov/public/project/AIRS/V7_L2_Product_User_Guide.pdf (accessed on 18 December 2023).

30. Blaisdell, J.M.; Farahmand, A.; Fetzer, E.J.; Fishbein, E.; Griffin, E.; Iredell, L.; Irion, F.W.; Kahn, B.H.; Kalmus, P.; Manning, E.; et al. AIRS Version 7 Level 2 Performance Test and Validation Report. Available online: https://docserver.gesdisc.eosdis.nasa.gov/public/project/AIRS/V7_L2_Performance_Test_and_Validation_report.pdf (accessed on 18 December 2023).

31. Kay, J.E.; L'Ecuyer, T.; Gettelman, A.; Stephens, G.; O'Dell, C. The contribution of cloud and radiation anomalies to the 2007 Arctic sea ice extent minimum. *Geophys. Res. Lett.* **2008**, *35*, L08503. [CrossRef]

32. Kay, J.E.; Gettelman, A. Cloud influence on and response to seasonal Arctic sea ice loss. *J. Geophys. Res. Atmos.* **2009**, *114*, D18204. [CrossRef]

33. Mace, G.G.; Zhang, Q.; Vaughan, M.; Marchand, R.; Stephens, G.; Trepte, C.; Winker, D. A description of hydrometeor layer occurrence statistics derived from the first year of merged Cloudsat and CALIPSO data. *J. Geophys. Res. Atmos.* **2009**, *114*, D00A26. [CrossRef]

34. Mace, G.G.; Benson, S.; Kato, S. Cloud radiative forcing at the Atmospheric Radiation Measurement Program Climate Research Facility: 2. Vertical redistribution of radiant energy by clouds. *J. Geophys. Res. Atmos.* **2006**, *111*, D11S91. [CrossRef]

35. Rossow, W.B.; Schiffer, R.A. Advances in Understanding Clouds from ISCCP. *Bull. Am. Meteorol. Soc.* **1999**, *80*, 2261–2288. [CrossRef]

36. Weare, B.C. Insights into the importance of cloud vertical structure in climate. *Geophys. Res. Lett.* **2000**, *27*, 907–910. [CrossRef]

37. Liu, X.; He, T.; Sun, L.; Xiao, X.; Liang, S.; Li, S. Analysis of Daytime Cloud Fraction Spatiotemporal Variation over the Arctic from 2000 to 2019 from Multiple Satellite Products. *J. Clim.* **2022**, *35*, 7595–7623. [CrossRef]

38. Meier, W.N.; Fetterer, F.; Savoie, M.; Mallory, S.; Duerr, R.; Stroeve, J. *NOAA/NSIDC Climate Data Record of Passive Microwave Sea Ice Concentration*; Version 3 [Data Set]; NSIDC: Boulder, CO, USA, 2017. [CrossRef]

39. Windnagel, A. NOAA/NSIDC Climate Data Record of Passive Microwave Sea Ice Concentration, Version 3 User Guide. Available online: https://nsidc.org/sites/nsidc.org/files/G02202-V001-UserGuide.pdf (accessed on 18 December 2023).

40. Reiser, F.; Willmes, S.; Heinemann, G. A New Algorithm for Daily Sea Ice Lead Identification in the Arctic and Antarctic Winter from Thermal-Infrared Satellite Imagery. *Remote Sens.* **2020**, *12*, 1957. [CrossRef]

41. Reiser, F.; Willmes, S.; Heinemann, G. Daily Sea Ice Lead Data for Arctic and Antarctic. 2020. Available online: https://doi.org/10.1594/PANGAEA.917588 (accessed on 27 December 2023).

42. Parkinson, C.L.; Comiso, J.C. On the 2012 record low Arctic sea ice cover: Combined impact of preconditioning and an August storm. *Geophys. Res. Lett.* **2013**, *40*, 1356–1361. [CrossRef]

43. Zhang, J.; Lindsay, R.; Schweiger, A.; Steele, M. The impact of an intense summer cyclone on 2012 Arctic sea ice retreat. *Geophys. Res. Lett.* **2013**, *40*, 720–726. [CrossRef]

44. Jeong, H.; Park, H.-S.; Stuecker, M.F.; Yeh, S.-W. Record Low Arctic Sea Ice Extent in 2012 Linked to Two-Year La Niña-Driven Sea Surface Temperature Pattern. *Geophys. Res. Lett.* **2022**, *49*, e2022GL098385. [CrossRef]

45. Zhu, J.; Yu, Y.; Guan, Z.; Wang, X. Dominant Coupling Mode of SST in Maritime Continental Region and East Asian Summer Monsoon Circulation. *J. Geophys. Res. Atmos.* **2022**, *127*, e2022JD036739. [CrossRef]

46. Ma, J.; Xie, S.-P.; Xu, H. Contributions of the North Pacific Meridional Mode to Ensemble Spread of ENSO Prediction. *J. Clim.* **2017**, *30*, 9167–9181. [CrossRef]

47. Chatterjee, S.; Raj, R.P.; Bertino, L.; Mernild, S.H.; Subeesh, M.P.; Murukesh, N.; Ravichandran, M. Combined influence of oceanic and atmospheric circulations on Greenland sea ice concentration. *Cryosphere* **2021**, *15*, 1307–1319. [CrossRef]

48. Li, X.; Krueger, S.K.; Strong, C.; Mace, G.G. Relationship Between Wintertime Leads and Low Clouds in the Pan-Arctic. *J. Geophys. Res. Atmos.* **2020**, *125*, e2020JD032595. [CrossRef]

49. Pagano, T.S.; Payne, V.H. The Atmospheric Infrared Sounder. In *Handbook of Air Quality and Climate Change*; Akimoto, H., Tanimoto, H., Eds.; Springer: Singapore, 2020; pp. 1–13.
50. Kahn, B.H.; Eldering, A.; Braverman, A.J.; Fetzer, E.J.; Jiang, J.H.; Fishbein, E.; Wu, D.L. Toward the characterization of upper tropospheric clouds using Atmospheric Infrared Sounder and Microwave Limb Sounder observations. *J. Geophys. Res. Atmos.* **2007**, *112*, D05202. [CrossRef]